文章编号：1001-9014(2026)01-0042-09

DOI:10.11972/j.issn.1001-9014.2026.01.006

# Study of dual-frequency-band millimeter-wave extended interaction klystron based on dual-2π mode

XU Che*, LU Jia-Ni, TANG Yong-Liang, TANG Xian-Feng*

(School of Physical Science and Technology, Southwest Jiaotong University, Chengdu 610031, China)

**Abstract**: This paper proposes a novel dual-frequency-band millimeter-wave extended interaction klystron amplifier (EIKA). It is primarily based on the multimode operating mechanism of dual-2π mode. This design integrates a broadband traveling-standing-wave mode input cavity with a dual-2π standing-wave mode output cavity, resulting in a compact slow-wave structure design that efficiently operates within a total circuit length of approximately 24 mm. Particle-in-cell simulation results reveal that under a 15.6 kV, 1 A electron beam and a uniform 0.6 T magnetic field, the device achieves output power for 183-1 024 W across a broadly 1.20 GHz bandwidth, spanning 93.76-94.96 GHz. Remarkably, it facilitates dual-band output in both lower-2π and upper-2π bands, delivering maximum gains of 37.09 dB (1 024.10 W at 93.90 GHz) and 35.75 dB (752.20 W at 94.84 GHz), with -3 dB bandwidths of 0.33 GHz and 0.20 GHz, respectively. The effectiveness for the dual-2π mode design is further confirmed through a cold-test experiment using the perturbation method. This experiment demonstrated typical dual-2π mode field distribution profiles, affirming the design´s efficacy.

**Key words**: extended interaction klystron (EIK), dual-band, multi-mode, millimeter waves, vacuum electronics

# 基于双2π模式的双频段毫米波扩展互作用速调管研究

徐 彻*, 卢佳妮, 唐永亮, 唐先锋*

(西南交通大学,物理科学与技术学院,四川 成都 610031)

**摘要**:本文基于双2π模式的多模工作机制,提出了一种新型的双频段毫米波扩展互作用速调管放大器(EIKA)。该设计由宽带行驻波模式输入腔和双2π驻波模式输出腔构成,形成紧凑的慢波结构设计,总电路长度约为24 mm。粒子仿真结果表明,在15.6 kV、1 A的电子束和0.6 T的均匀磁场作用下,该器件在93.76~94.96 GHz的1.20 GHz带宽可以达到183~1 024 W的输出功率。值得注意的是,它可以实现低2π和高2π频段的双频输出,在-3 dB带宽分别为0.33 GHz和0.20 GHz的情况下,最大增益为37.09 dB(93.90 GHz时为1 024.10 W)和35.75 dB(94.84 GHz时为752.20 W)。通过微扰法-冷测实验,得到了典型的双2π模场分布曲线,进一步验证了双2π模设计的有效性。

**关 键 词**:扩展互作用速调管;双频段;多模;毫米波;真空电子学

**中图分类号**:TN129 **文献标识码**:A

## Introduction

The landscape of future wireless communication systems is evolving rapidly, encompassing a growing range of frequency bands and standards[1,2]. The diversity of these systems necessitates that all components, especially power amplifiers (PAs) known for their high peak power, are flexible enough to operate across multiple modes[3,4]. This emerging requirement poses substantial challenges to PA systems.

**Received date**: 2024-10-16, **revised date**: 2025-02-21 **收稿日期**:2024-10-16,**修回日期**:2025-02-21

**Foundation items**: Supported by the Fundamental Research Funds for the Central Universities (2682023CX076), the Natural Science Foundation of Sichuan, China (2024NSFSC1432), the National Natural Science Foundation of China (62301459).

**Biography**: XU Che (1992-), male, Chengdu, China. Research area involves terahertz electronic vacuum devices, high power microwave devices. E-mail: xuche@swjtu.edu.cn.

* **Corresponding authors**: E-mail: xuche@swjtu.edu.cn, txf_2012@163.com

In the realm of millimeter-wave microwave-RF devices, including extended interaction klystron amplifiers (EIKAs)[5-12], traveling-wave tube amplifiers (TWTAs)[13, 14], and solid-state integrated-circuit RF power amplifiers (SSPAs)[15, 16], there is a broad spectrum of mature applications spanning from radar and electronic countermeasures to military communication and civilian telecom. To meet the practical requirements for multi-band and broadband operation, these devices are continuously exploring multimode capabilities. A well-established example is the dual-mode TWT, which can operate in both upper and lower modes. For instance, the X-band dual-mode TWT developed by Varian Associates for airborne countermeasures achieves 500 W of continuous wave power and 700 W of pulse power in the 9.6-9.8 GHz band[17], with gains of 40.5 dB and 30.5 dB in lower and upper modes, respectively. Recently, the University of California proposed a dual-mode TWT operating at 0.2 THz[18], achieving 10 W of continuous wave power and 100 W of pulse output power in the 190-210 GHz band. Another example is the solid-state integrated-circuit RF power amplifier. For instance, Robin Kalyan and colleagues from the Indian Institute of Technology designed a dual-frequency power amplifier operating at 1.6-2.3 GHz with an output power of 10 W[19]. Renato Negra and his team from RWTH Aachen University developed a multi-band bias network concurrent four-band power amplifier, achieving 10W output power in the 1.49-2.65 GHz range[20]. These results are promising, but thermal management and long-term stability of the devices may pose challenges in high-power applications. As for EIK research, it is primarily based on single-band models. For instance, a dual-mode extended interaction oscillator (EIO) circuit operating at 93.7-94.2 GHz, capable of switching between modes through electrical tuning[21]. However, the exploration into multi-modal operation of EIKA is still an emergent field. Indeed, despite the mature applications of multi-band devices based on TWTs and solid-state RF power amplifiers, they still face challenges in terms of power (gain)[22], solving processes, and circuit complexity.

The pursuit of both broad-and-multi-band and high gain in millimeter-wave vacuum electronic devices (VEDs) through relatively straightforward and easily manufacturable circuit designs has been a focal area of research in recent years. To combine the relative advantages of bandwidth and gain found in TWTs and klystrons respectively, this paper proposes a novel dual-frequency-band EIK model. This model features a compact two-cavity configuration, incorporating a traveling-standing-wave input cavity and a dual-2π mode standing-wave output cavity, designed to deliver enhanced gain levels in two frequency bands. The structure, as shown in Fig. 1, offers the following advantages: 1) The use of a compact traveling-standing-wave mode input cavity for primary signal amplification, achieving a -3 dB bandwidth of 0.72 GHz; 2) The establishment of a dual-frequency-band standing-wave output cavity based on dual-2π modes, utilizing the high characteristic impedance $R/Q$ of the standing-wave mode to effectively enhance the gain level over a certain circuit length; 3) The novel hybrid action of traveling-and-standing wave modes allows for signal amplification in two frequency bands without the need for electrical tuning.

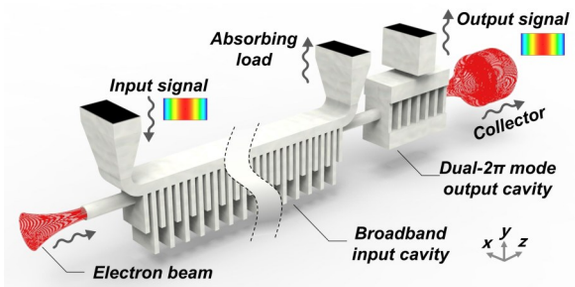


Fig. 1 The three-dimensional schematic diagram of the proposed EIK.
图1 双频段EIK三维结构示意图

## 1 High-frequency characteristics

### 1.1 Input cavity

In this study, a more compact two-cavity structure is proposed for the EIKA. To achieve broadband primary signal amplification, establishing a suitable input cavity with a wide frequency response range is essential. It should be emphasized that the incorporation of a traveling-wave amplification mechanism within the extended interaction circuit can effectively broaden the bandwidth[23-25]. Therefore, a broadband input cavity with traveling-wave characteristics has been adopted. Its design, depicted in Fig. 2, comprises an input port, a load port, a coupling cavity, an alternating array of 21 long slots and 22 short slots, along with a beam channel traversing these gaps. The load waveguide is designed to absorb the excess energy from the traveling wave amplification process. The fundamental structure and characteristic parameters of this cavity are detailed in Table. I.

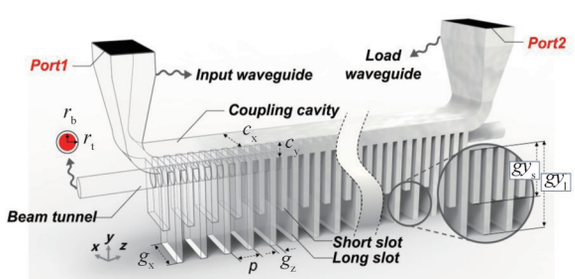


Fig. 2 The three-dimensional schematic diagram of the broadband input cavity.
图2 宽带输入腔的三维结构示意图

Based on the proposed structure of the traveling-wave broadband input cavity, its high-frequency intrinsic characteristics were analyzed. Based on the high-frequency intrinsic characteristics of the input cavity, as shown in Fig. 3(a)-3(c), there are three continuous transitional traveling wave modes (2π, π/20, 2π/20)

**Table 1 Typical structural-and-characteristic parameters for the proposed input cavity**
**表 1 输入腔的典型结构参数和特征参数**

| Symbol/Quantity | Value | Symbol/Quantity | Value |
|---|---|---|---|
| $c_x$ | 1.80 mm | $p$ | 0.80 mm |
| $c_y$ | 0.50 mm | Filling factor | 0.64 |
| $g_x$ | 1.70 mm | Long slot number | 21 |
| $g_{yl}$ | 3.28 mm | Short slot number | 22 |
| $g_{ys}$ | 1.30 mm | Syn. voltage | ~15.6 kV |
| $g_z$ | 0.22 mm | -3dB bandwidth | 0.72 GHz |
| Tunnel radius $r_t$ | 0.30 mm | $f_0$ (center) | 94.5 GHz |
| Beam radius $r_b$ | 0.24 mm | Guiding $B$-field | 0.6 T |

that support the field distributions. As observed in Fig. 3(a), the traveling wave mode, functioning at the edge of the passband in the slow-wave structure, incorporates elements of a standing wave, thus forming a hybrid traveling-standing wave configuration. The determination of these traveling-standing-wave modes is based on the phase angle shift between the long slots in the field distribution, identified using the resonance method, as illustrated in Fig. 3(c) and 4(a)-4(c). Particularly in Fig. 4(a)-4(c), the different periodic phase variations result in the 2π, π/20, and 2π/20 modes having 1, 2, and 3 envelope counts, respectively. The continuous phase-transition allows for the coexistence of the three transitional modes within the cavity, thereby enabling effective electronic velocity modulation within the corresponding frequency band. It is noteworthy that all three traveling-standing-wave modes from 2π to 2π/20 operate under the fundamental-transverse $TM_{11}$ mode. Correspondingly, the normalized phase velocity curve in Fig. 3(b) intersects with the 15.6 kV voltage line near the synchronous phase velocity range of the above three traveling-standing-wave modes, establishing the basic conditions for multimode continuous operation of beam-wave interaction[26]. However, it is crucial to balance bandwidth and gain, excessively broadening bandwidth in pursuit of traveling-wave properties may not favor compact circuit design while maintaining specific gain levels. From the perspective of characteristic impedance, the transitions from the π/20 to 2π/20 modes in traveling-wave operation are also closely aligned with the standing-wave 2π mode, facilitating higher gain and compact circuit design over a certain length.

The output gain curves derived from the three-dimensional electromagnetic simulations, which involved the interaction between the meticulously designed slow-wave structure and an electron beam of 15.6 kV and 1 A, are depicted in Fig. 3(d). In these simulations, the metallic components were modeled using oxygen-free copper with an electrical conductivity of $2\times10^7$ S/m. For analytical clarity, the input signal was standardized at 0.2 W. The results indicate that the maximum gain of the input cavity is 31.76 dB at 94.50 GHz, with a corresponding -3 dB bandwidth of 0.72 GHz across the 94.14-94.86 GHz range. As illustrated in Fig. 5(a), the signal frequencies at both the input and output ports are consistently stable and well-aligned at 94.50 GHz, indicating effective signal isolation. Notably, the input signal amplitude remains stable, showing no signs of reflection-induced oscillations. Similarly, Fig. 5(b) confirms that the output frequency remains consistent over time, firmly locked by the input frequency settings.

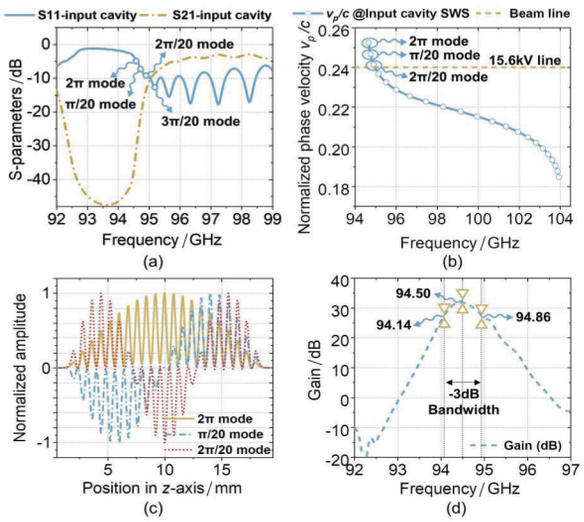


Fig. 3 The proposed broadband input cavity features curves: (a) S-parameters versus frequency; (b) normalized phase velocity versus frequency; (c) normalized amplitude of electric field strength along the centerline for the beam tunnel; (d) typical output gain versus input/output frequency.
图3 宽带输入结构特性曲线:(a) S参数与频率的关系;(b)归一化相速度与频率的关系;(c)沿束通道中心的归一化电场强度幅度;(d)典型输出增益与输入/输出频率关系

It should be recognized that such bandwidth and gain levels are achievable with existing folded waveguide structures, potentially offering even broader bandwidths[27, 28]. In comparison to typical folded waveguides[28], the proposed broadband extended interaction input cavity distinguishes itself with its high gain per unit length and compact slow-wave structure, measuring approximately 17 mm in axial length.

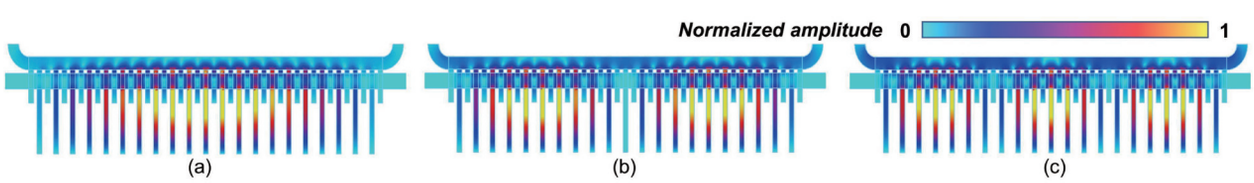


Fig. 4 Contour maps of the electric field distribution: (a) 2π mode; (b) π/20 mode; (c) 2π/20 mode
图4 电场分布图:(a) 2π模;(b) π/20模;(c) 2π/20模

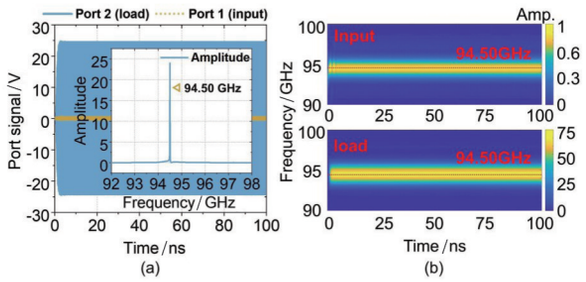


Fig. 5 (a) The amplitude and spectrum for the input and load signals; (b) the corresponding time-frequency analysis diagrams.
图5 输入信号和负载信号的振幅和频谱图;(b) 时频分析

### 1.2 Dual-2π mode output cavity

Typically, EIKs are operated in the single 2π mode, specifically in the $TM_{11}$ transverse mode, to maximize gain. However, although the existence of two $TM_{11}$ modes exhibiting periodic 2π phase shifts has been recognized[21], their amplification properties and multi-band operation capabilities have not yet been investigated. The complexity of researching these modes stems primarily from the challenges in synchronizing the phase velocity with the electron beam and in optimizing multiple mode characteristics, such as the $R/Q$, and external quality factor $Q_l$.

To simultaneously achieve high gain performance in two bands, a cavity with strong standing-wave properties was established. This design leverages the high characteristic impedance of the standing-wave mode, resulting in a compact and efficient output cavity with seven gaps. This extended interaction output cavity is crucial for the dual-frequency-band EIKA, featuring a total slow-wave structure length of ~5mm. The configuration includes an output port, seven interaction gaps, two coupling cavities positioned on each side of these gaps, and a central beam tunnel piercing through the gaps. Detailed descriptions for the structure and characteristic parameters are presented in Fig. 6 and Table. II.

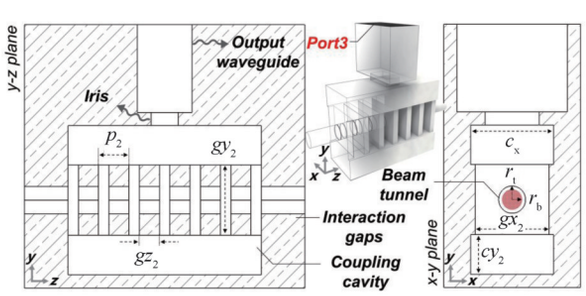


Fig. 6 Three-dimensional and cross-sectional diagrams for the proposed dual 2π mode output cavity
图6 双2π模输出腔的三维图和截面图

Fig. 7 illustrates the dispersion relation for the resonant slow-wave structure of the output cavity, confirming that both 2π modes adhere to the synchronization condition where electron velocity slightly exceeds the phase velocity. The figure also showcases the electric field distributions for these modes: the higher-frequency upper-band 2π mode and the lower-frequency lower-band 2π mode, each aligning with the 2π principle in their phase variations (co-directional). The reflection coefficients for the circuit, $S_{11}$, as revealed in Fig. 8 and 9(a), shows a pronounced responsiveness to both 2π modes when the circuit is utilized as a load. Moreover, the 3dB bandwidth of the $S_{11}$ curve can be finely tuned by adjusting the dimension $cx$, facilitating the attainment of an optimal $Q_l$, calculated as

$$Q_l = \frac{f_r}{\Delta f_b} \quad , \quad (1)$$

where $f_r$ represents the resonant frequency, and $f_b$ is the bandwidth measured from the minimum value to the upper 3dB point. The upper-2π mode and lower-2π mode are characterized by external quality factors $Q_{l1}$=371.4 and $Q_{l2}$=589.3, respectively. Specifically, it is observed that the field distributions for the upper and lower 2π modes depicted in Fig. 7 predominantly reside within the coupled cavities and the interaction gaps, respectively. Hence, they can be likened to the "cavity mode" and "slot mode" found in coupled cavity traveling wave tubes, as referenced in[26]. Considering the close frequency proximity of these two modes, they can also be characterized as quasi-degenerate modes. When the width of the coupling cavity is further increased from the original design, the higher-2π-mode vanishes.

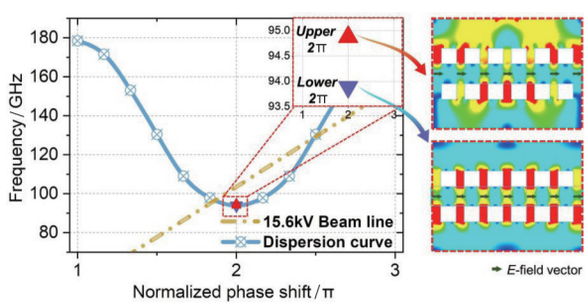


Fig. 7 Dispersion curve for the dual 2π mode output cavity, along with electric field contour maps for both 2π modes.
图7 双2π模式输出腔的色散曲线,以及双2π模式的电场分布图

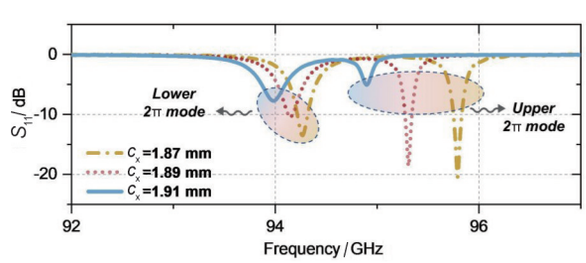


Fig. 8 $S_{11}$ curves at various coupling cavity widths, $c_x$
图8 $S_{11}$随耦合腔宽度$c_x$的变化

For further understanding of the beam-wave interaction capability of potential modes in the cavity, the intrinsic characteristic curves of the cavity were studied, as shown in Fig. 9(b) to 9(d). As expected, strong $R/Q$

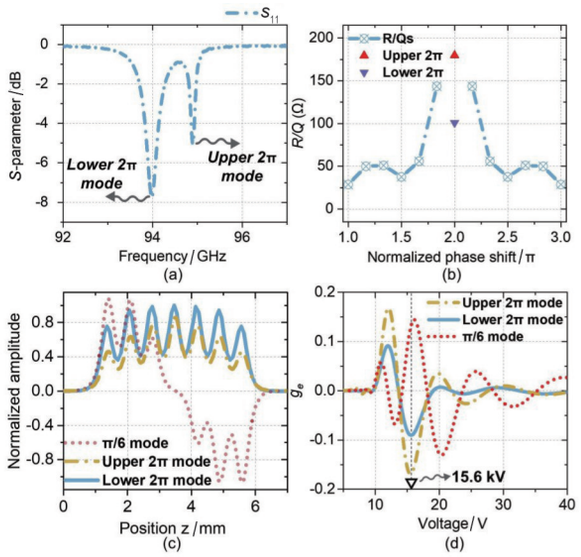


Fig. 9 Curves analyzing the Intrinsic characteristics of the cavity: (a) the $S_{11}$ Curve; (b) *R/Q* variation with phase shift; (c) comparative field distribution curves between potential operating modes; (d) the beam-loading conductance versus voltage

图9 腔体固有特性的曲线分析:(a) $S_{11}$曲线,(b) *R/Q*随相移的变化曲线;(c)潜在工作模式的场分布曲线对比;(d)电子束电导随电压的变化曲线

**Table 2 typical structural-and-characteristic parameters for the proposed output cavity**

**表2 输出腔的典型结构和特征参数**

| Symbol/Quantity | Value | Symbol/Quantity | Value |
|---|---|---|---|
| $c_{x2}$ | 1.91 mm | $p_2$ | 0.70mm |
| $c_{y2}$ | 0.90 mm | gap number $N$ | 7 |
| $g_{x2}$ | 1.70 mm | $f_1$ (lower 2π) | 93.88GHz |
| $g_{y2}$ | 1.60 mm | $f_2$ (upper 2π) | 94.87GHz |
| $g_{z2}$ | 0.24mm | Total length of SWS | ~24mm |

values were observed near the 2π standing-wave modes. Specifically, the *R/Q* values for the upper-2π and lower-2π modes were 179.80 and 100.85 Ω, respectively, demonstrating the benefits of utilizing the 2π standing-wave mode for beam-wave interactions. Comparatively, all other modes, except for the π/6 mode, exhibited *R/Q* values below 60 Ω. Notably, the π/6 mode, despite being a potential parasitic mode, registered an *R/Q* of 143.55 Ω. This prompted an analysis of the high-frequency characteristics under beam-loaded conditions. Fig. 9(c) presents the field distribution patterns for the upper 2π, lower 2π, and π/6 modes, where both the upper and lower-2π modes display envelope waveforms featuring seven peaks and six valleys. This pattern aligns with the 2π-phase shifts between periods, as analyzed in Fig. 7, and is characteristic of the 2π modes. The corresponding beam-loading conductance $g_e$ for these field distributions is analyzed in Fig. 9(d). Under the beam-loading, only the two 2π modes are evident, owing to their near-identical synchronous phase velocities, enabling synchronization at a voltage of 15.6 kV. The π/6 mode, with its positive $g_e$, suggests that energy would be transferred from the electromagnetic field back to the electron beam, thereby inhibiting its amplification. The $g_e$ can be expressed as

$$g_e = \frac{G_e}{G_0} = \frac{1}{4} G_0 \beta_e \left[ \frac{M^2(\beta_e + \beta_q) - M^2(\beta_e - \beta_q)}{2\beta_q} \right], \quad (2)$$

where the $G_0$ stands for the DC beam conductance, $I_0/U_0$[29]. $\beta_e = \omega/v_e$ and $\beta_q = \omega_q/v_e$ are the propagation constants of the DC beam and reduced plasma respectively, which are determined by the RF radian frequency $\omega$, reduced-plasma angular frequency $\omega_q$, and DC beam velocity $v_e$. The coupling coefficient $M$ can be obtained by:

$$M(\beta_e) = \frac{\int_{-\infty}^{+\infty} E(z)\exp(-j\beta_e z)dz}{\int_{-\infty}^{+\infty} |E(z)|dz}, \quad (3)$$

## 2 Beam-wave interactions

Extensive 3D electromagnetic simulations based on CST[30], were carried out on an EIKA, featuring a total interaction circuit length of ~24 mm. This device, integrating the proposed broadband traveling-wave mode input cavity with a cascaded dual 2π mode standing-wave output cavity (as illustrated in Fig. 1), was rigorously calculated to assess its dual-frequency-band output capabilities. In addressing the challenges of W-band ohmic losses and electron beam transmission, both the electrical conductivity and magnetic field strength were set consistently at $2\times10^7$ S/m and 0.6 T uniformly. The 0.6 T uniform magnetic field can be implemented using a neodymium-iron-boron (NdFeB) permanent magnet configuration, as outlined in.[31] These exacting conditions were essential in ensuring the reliability and accuracy of our simulation results.

Observations were made under a set of specific conditions: input power of 0.2 W, an electron beam with parameters 15.6 kV and 1 A (552 A/cm$^2$), and input frequencies set at 93.90 GHz for the lower-2π mode and 94.84 GHz for the upper-2π mode. These conditions led to notable modulation of the electron beam. As depicted in Fig. 10(a) and 10(b), which characterize the extent of energy dispersion, velocity modulation occurs within the input cavity without a substantial reduction in the average power of the electron beam. In contrast, within the output cavity, the average electron velocity in both the lower and upper 2π modes reduced by respectively 13.7% and 18.0% from the initial 15.6 kV, signifying the transformation of electron kinetic energy into microwave energy. Regarding the electron transmission rate, simulations have confirmed that the electron transmission rate is at 100% prior to oscillation-starting, and the electron transmission rate at the power saturation state is 98.9%.

Port signal-spectra, as shown in Fig. 11(a) and 11(c), and time-frequency analyses, conducted using wavelet transform methods and depicted in Fig. 11(b) and 11(d), indicated stable operation in both 2π mode bands with pure spectra under input frequency locking. The frequency locking time for the lower-2π mode was

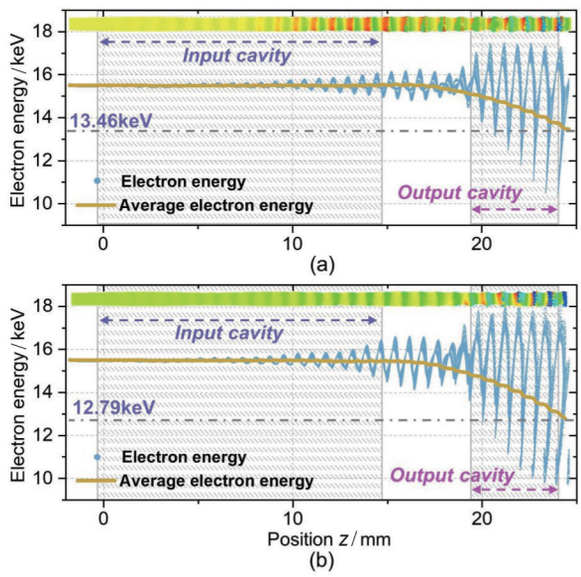


Fig. 10 Energy dispersion diagrams for the proposed EIKA at 93.90 GHz in the lower 2π mode and at 94.84 GHz in the upper 2π mode
图 10 93.90 GHz的低2π模式和94.84GHz的高2π模式下能量色散图

less than 2ns, and for the upper-2π mode, it was less than 3 ns.

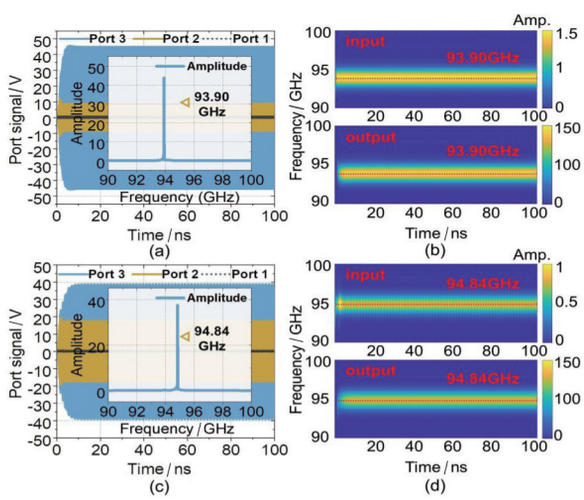


Fig. 11 PIC simulation results for the dual-band EIK: (a) port signal diagrams and (b) time-frequency contourmaps at 93.90GHz in the lower-2π mode; (c) port signal diagrams and (d) time-frequency contourmaps at 94.84GHz in the upper-2π mode
图 11 双频EIK的PIC仿真结果: 93.90 GHz的低2π模式(a)端口信号图和(b)时频轮廓图; 94.84 GHz的高2π模式(c)端口信号图和(d)时频轮廓图

To evaluate the performance of the proposed EIKA under voltage tuning, over 1 000 simulations were conducted. Fig. 12(a) presents a contour map of output power as a function of both voltage and input frequency, demonstrating that modes can be locked by adjusting the input frequency across different voltages, thereby also stabilizing the output frequency. These simulations demonstrate that within the lower 2π mode, a voltage range spanning 15.6-16.6 kV can reliably generate an output power in excess of 1000 W. In parallel, for the upper 2π mode, a voltage range from 15.0 to 16.8 kV is capable of consistently delivering an output power surpassing 500 W. Fig. 12(b) and 12(c) display the variations in gain and power across frequencies under identical operational conditions (15.6 kV). Optimistic results were observed, with the EIKA demonstrating broadband amplification performance exceeding 183 W across a 1.20 GHz bandwidth from 93.62 to 94.94 GHz. Within this frequency range, as the input/output frequency increases, the electric field distribution will exhibit a uniform transition from the lower 2π mode to the upper 2π mode, with both 2π-modes′ field distributions consistent with Fig. 7. In this context, the mode distribution shown in Fig. 12(c) is obtained by monitoring the electric field in the PIC simulation. These results also confirm that within the 14-18 kV voltage range, the output frequency can be effectively locked to the input frequency, demonstrating the amplification performance across two frequency bands. Specifically, the range of 93.82-94.15 GHz corresponding to the lower-band 2π mode exhibited a maximum gain of 37.09 dB (1024.10 W) and a -3 dB bandwidth of 0.33 GHz; the range of 94.72-94.92 GHz corresponding to the upper-band 2π mode exhibited a maximum gain of 35.75 dB (752.20 W) and a -3 dB bandwidth of 0.20 GHz. At the central frequencies for the dual 2π mode, the single-cavity gain provided by this standing wave output cavity is 6.82 dB and 14.25 dB, respectively.

The advancement in the physical mechanism for these results herein lies in the achievement of stable dual-frequency band outputs, as opposed to the ′dual power

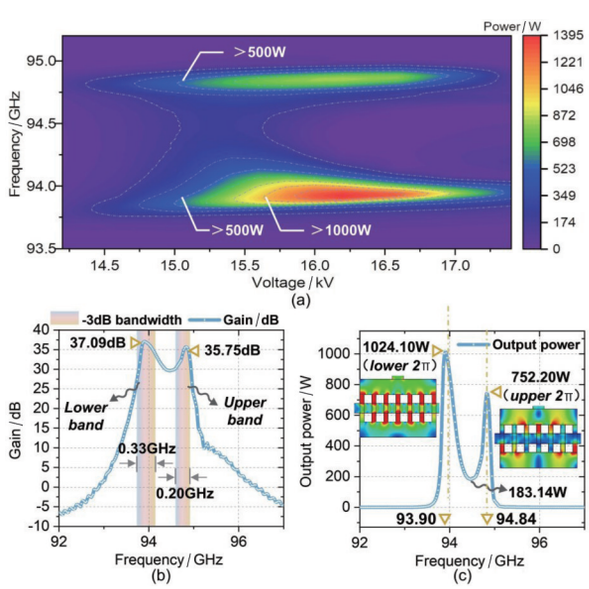


Fig. 12 (a) Contour map of the output power for the dual-band EIKA as a function of both frequency and voltage; (b) the gain and (c) power as functions of frequency at 15.6 kV
图 12 (a)双频EIKA输出功率随频率和电压变化的轮廓图; 15.6 kV时(b)增益随频率变化图;(c)功率随频率变化图

mode′ operation of dual-mode traveling wave tubes[17, 18], without the need for the gate-control required by the latter. In terms of output power, compared to multi-band solid-state integrated-circuit RF power amplifiers, the power output has been increased by approximately two orders of magnitude from 10W [19, 20]. For comparative analysis, the performance parameters of several typical EIKs and SSPAs are summarized in Table. III.

**Table 3 The operating parameters of several typical vacuum electronic devices and solid-state devices**
**表3 几个典型的真空电子器件和固态器件的工作参数**

| Device | Frequency band | Bandwidth (MHz) | Efficiency (%) | Multimode operation |
|---|---|---|---|---|
| EIK[5] | W-band | 120 | 15.6 | No |
| EIO[12] | W-band | - | 3.5 | No |
| EIO[21] | W-band | - | 8.8/5.2 | Yes |
| SSPA [20] | L-band | ~400 | >55 (only~ 10 W) | Yes |
| This paper | W-band | 330/200 | 6.6/4.9 | Yes |

## 3 Perturbation experiments

The studies referenced above all assume the existence of the dual-2π mode, but this premise has not been empirically verified through experimental reports. The authors explored various measurement methodologies[32, 33], including the coaxial probe technique, ultimately converging on the particle-perturbation method to assess the field distribution in a fabricated dual-2π mode extended interaction output cavity. This method entailed the utilization of a dielectric tether, to which a perturbing mass was attached, thereby inducing a disturbance in the extended interaction circuit. The impact of this disturbance on the *S*11 parameter was quantitatively analyzed using a vector network analyzer (VNA). The movement of the perturbing mass and the corresponding frequency shift in the *S*11 measurement were observed to deduce the field strength at the measurement point. The experiment aims to verify the presence of the *Ez* distribution of the dual 2π mode along the central axis of the beam tunnel, providing critical data for the design of dual-frequency-band EIKA systems.

Fig. 13(a) shows the fundamental configuration of the suggested particle perturbation experiment. In this setup, for improved measurability and operational feasibility of the perturbation technique, the dual-mode cavity is proportionately enlarged to a 34 GHz structure (shown in Fig. 13(b)), featuring a beam channel with a radius of 0.5 mm. Note that, the above setup (enlarged cavity) is required, as to ensure the accuracy of the perturbation tests, a considerable number of such perturbation tests are currently conducted at frequencies below 10GHz[34, 35]. A symmetric assembly approach can be adopted for the practical implementation of the 94 GHz slow-wave circuit.

When considering a test setup with minimal surface losses, the frequency shift in a resonant cavity due to a small dielectric perturbation can be calculated using the lossless field solution. Assuming the impact of the magnetic field can be neglected and the electric field within the dielectric is uniform[36], a simplified perturbation formula can be derived by[37]

$$\frac{\Delta f}{f_0} \approx \left(\frac{4}{3}\pi a^3 \cdot \frac{3(1-\varepsilon_r)}{2+\varepsilon_r} \cdot \frac{\varepsilon_0}{4W}\right)\left|E_0\right|^2 \quad , \quad (4)$$

where $W$ and $a$ represent the power capacity within the cavity and the radius for the perturbing mass, respectively.

From Eq. (4), it can be inferred that the frequency deviation is directly proportional to the square of the electric field strength $E_0$, reflecting the distribution of the electric field strength.

The above discussion reveals several typical issues in the current experimental setup that warrant improvement in future. These include: 1) The perturbation experiment neglects the influence of the slender dielectric tether; 2) The relative magnetic permeability $\mu_r$ is approximated as 1.

The simulated results for the field distributions of the corresponding test structure are shown in Fig. 14 (a), where the presence of the dual 2π mode is observed. The $S_{11}$ curve is depicted in Fig. 14 (b), showing a basic consistency between simulation and test curves. The test results reveals a reduced frequency spacing for the dual-2π mode in comparison to the simulated predictions, a difference predominantly ascribed to inaccuracies inherent in the fabrication process. To verify that the test curve obtained from $S_{11}$ corresponds to the dual 2π mode, a perturbation frequency deviation experiment was conducted. Utilizing 120 sampling points and a perturbing particle with a 0.4 mm radius and a $\varepsilon_r$ of ~7, both the simulated and experimental curves for the frequency deviation were plotted, as shown in Fig. 14 (c) and 14 (d). These curves are largely congruent, exhibiting an envelope with seven peaks and six valleys, characteristic of the 2π mode. The maximum frequency deviations recorded for the upper and lower 2π modes were 149.65 MHz and 28.00 MHz, respectively, with their relative errors in comparison to the simulation in Fig. 14(c) calculated at 6.3% and 1.2%. This correlation validates the design rationale behind the dual-2π mode mecha-

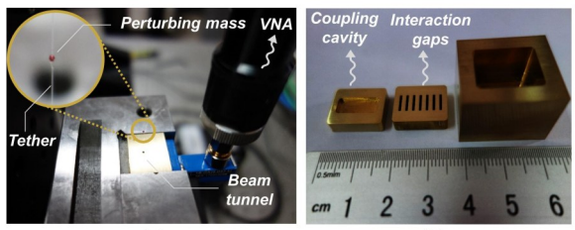


(a) (b)

Fig. 13 (a) Basic setup for the particle perturbation experiment; (b) the multi-layer assembly structure of the dual-mode output cavity
图13 (a)质点微扰实验的基本设置;(b)双模输出腔的多层组装结构

nism.

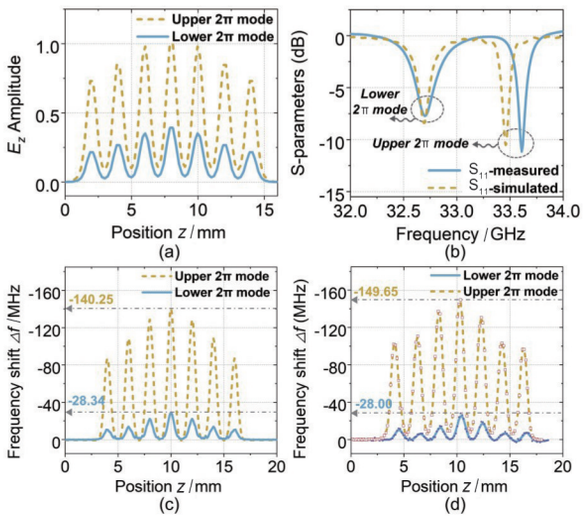


Fig. 14 Simulation and test curves for the fabricated 34 GHz structure: (a) Simulated results of the electric field distribution; (b) comparison curves for S-parameters; (c) simulated curves of perturbation frequency deviation; (d) experimental curves of perturbation frequency deviation

图 14 34 GHz结构的模拟与实验曲线:(a)电场分布模拟结果;(b)S参数对比曲线;(c)扰动频率偏差模拟曲线;(d)扰动频率偏差实验曲线

It should be noted that these perturbation results, indicative of a reduced frequency, are attributed to the larger inner surface area of the cavity caused by adding the perturbing body. This expansion increases the capacitance, consequently leading to a negative $\Delta f$.

## 4 Conclusions

To achieve a rational design of a dual millimeter-wave band high-power coherent radiation source, this paper conducted extensive research involving simulations and cold tests. For a more compact configuration, a broadband traveling-standing-wave mode extended interaction input cavity and a dual-2π standing-wave mode output cavity were adopted, with the total length of the beam-wave interaction structure being approximately 24 mm. Factors such as electron beam parameters (15.6 kV, 1 A), magnetic field strength (0.6 T uniformly), and electrical conductivity ($2\times10^7$ S/m) were meticulously integrated into our three-dimensional electromagnetic simulations for enhanced engineering practicality. A dual-2π output cavity, based on multilayer manufacturing technology, was tested using the perturbation method, confirming the rationality of the dual-2π mode design and revealing the corresponding dual-2π mode electric field distribution.

Ultimately, the dual-frequency-band EIKA circuit is anticipated to achieve frequency locking and output power exceeding 183 W within a 1.20 GHz bandwidth at 93.76-94.96 GHz; with peak output powers in the upper-band 2π mode and lower-band 2π mode reaching 1024.10 W (93.90 GHz, 37.09 dB) and 752.20 W (94.84 GHz, 35.75 dB), respectively, and -3 dB bandwidths of 0.33 and 0.20 GHz. It should be noted that, according to the results presented, the power levels in the two frequency bands are comparable. By optimizing the characteristic parameters of the two 2π modes, it is also feasible to achieve a dual-power-mode design in the future, akin to dual-mode traveling wave tube amplifiers (TWTAs).

The effective utilization of the dual-2π mode facilitates the advancement of vacuum electronic amplifiers towards higher gains and multi-band capabilities, supporting a wider range of multi-band, frequency-hopping communication applications, and more.

## References

[1] FENG J J, LI X H, HU J N, et al. General Vacuum Electronics [J]. JOURNAL OF ELECTROMAGNETIC ENGINEERING AND SCIENCE, 2020, 20(1): 1-8.
[2] JIN Qi, GENGZhi-Hui, ZHANG Jian, et al. Design of high-frequency circuit for W-band CW sheet beam extended-interaction klystron [J]. J. Infrared Millim.Waves, 2022, 41(6):1030-1036.
金琦 耿, 张健等. W波段连续波带状注扩展互作用速调管高频电路的设计 [J]. 红外与毫米波学报, 2022, 41(6):1030-1036.
[3] KOROLEV A N, ZAITSEV S A, GOLENITSKIJ, II, et al. Traditional and novel vacuum electron devices [J]. IEEE TRANSACTIONS ON ELECTRON DEVICES, 2001, 48(12): 2929-37.
[4] MOHAMED A M M, BOUMAIZA S, MANSOUR R R. Reconfigurable Doherty Power Amplifier for Multifrequency Wireless Radio Systems [J]. IEEE TRANSACTIONS ON MICROWAVE THEORY AND TECHNIQUES, 2013, 61(4): 1588-98.
[5] XIE Bing-Chuan, ZHANG Rui, WANG Huan-Huan, et al. Design of W-band high-order mode extended interaction klystron based on novel multi-gap cavity [J]. J. Infrared Millim.Waves, 2023, 42(4): 504-509.
谢冰川 张, 王欢欢等. 基于新型多间隙谐振腔的W波段高次模式扩展互作用速调管设计[J]. 红外与毫米波学报, 2023, 42(4): 504-509.
[6] PASOUR J, WRIGHT E, NGUYEN K T, et al. Demonstration of a Multikilowatt, Solenoidally Focused Sheet Beam Amplifier at 94 GHz [J]. IEEE TRANSACTIONS ON ELECTRON DEVICES, 2014, 61(6): 1630-6.
[7] ZHANG F, ZHAO Y Q, RUAN C J. A High-Power and Broadband G-Band Extended Interaction Klystron Based on Mode Overlap [J]. IEEE TRANSACTIONS ON ELECTRON DEVICES, 2022, 69(8): 4611-6.
[8] NAIDU V B, GOPE D, DATTA S K. Enhancement of Bandwidth of an Extended Interaction Klystron by Symmetric Loading [J]. IEEE TRANSACTIONS ON PLASMA SCIENCE, 2022, 50 (12): 5018-22.
[9] CAI J C, SU Z X, PEAUGER F, et al. Exploratory Study on High-Efficiency High-Power W-Band Klystron Based on Kladistron Technology [J]. IEEE TRANSACTIONS ON PLASMA SCIENCE, 2023, 51(2): 386-91.
[10] WANG J X, WAN Y X, XU D Q, et al. Performance and Experimental Progress of a Compact W-band High Average Power Sheet Beam Extended Interaction Oscillator [J]. IEEE ELECTRON DEVICE LETTERS, 2023, 44(1): 144-7.
[11] SHU G X, ZHANG L, YIN H, et al. Experimental demonstration of a terahertz extended interaction oscillator driven by a pseudospark-sourced sheet electron beam [J]. APPLIED PHYSICS LETTERS, 2018, 112(3):
[12] SHU G X, YIN H, ZHANG L, et al. Demonstration of a Planar W-Band, kW-Level Extended Interaction Oscillator Based on a Pseudospark-Sourced Sheet Electron Beam [J]. IEEE ELECTRON DEVICE LETTERS, 2018, 39(3): 432-5.
[13] CHERNIN D, ANTONSEN T M, VLASOV A N, et al. 1-D Large Signal Model of Folded-Waveguide Traveling Wave Tubes [J]. IEEE TRANSACTIONS ON ELECTRON DEVICES, 2014, 61 (6): 1699-706.
[14] SHIN Y M, BARNETT L R, LUHMANN N C. Phase-Shifted Traveling-Wave-Tube Circuit for Ultrawideband High-Power Submillime-

ter-Wave Generation [J]. IEEE TRANSACTIONS ON ELECTRON DEVICES, 2009, 56(5): 706-12.
[15] KALYAN R, RAWAT K, KOUL S K. Reconfigurable and Concurrent Dual-Band Doherty Power Amplifier for Multiband and Multistandard Applications [J]. IEEE TRANSACTIONS ON MICROWAVE THEORY AND TECHNIQUES, 2017, 65(1): 198-208.
[16] GILASGAR M, BARLABé A, PRADELL L. High-Efficiency Reconfigurable Dual-Band Class-F Power Amplifier With Harmonic Control Network Using MEMS [J]. IEEE MICROWAVE AND WIRELESS COMPONENTS LETTERS, 2020, 30(7): 677-80.
[17] W. R. AYERS G V M, J. SCHRIEVER, AND J. RUETZ. High Power Dual Mode Coupled-Cavity Twt [C]. 1976 International Electron Devices Meeting. 1976: 256-9.
[18] ZHENG Y, GAMZINA D, LUHMANN N C. 0.2-THz Dual Mode Sheet Beam Traveling Wave Tube [J]. IEEE TRANSACTIONS ON ELECTRON DEVICES, 2017, 64(4): 1767-73.
[19] KALYAN R, RAWAT K, KOUL S K, et al. Design of Reconfigurable Concurrent Dual-Band Power Amplifiers using Reconfigurable Concurrent Dual-Band Matching Network [C]. 2016 IEEE MTT-S INTERNATIONAL WIRELESS SYMPOSIUM (IWS). 2016.
[20] XUAN A N, NEGRA R, IEEE. Design of concurrent multiband biasing networks for multiband RF power amplifiers [C]. 2012 42ND EUROPEAN MICROWAVE CONFERENCE (EUMC). 2012: 1-4.
[21] CHANG Z W, MENG L, YIN Y, et al. Study of a Dual-Mode W-Band Extended Interaction Oscillator [J]. IEEE TRANSACTIONS ON ELECTRON DEVICES, 2018, 65(6): 2620-5.
[22] SUMATHY M, REDDY S U M, BHAT K S. Estimation of RF-wall loss in slow-wave structures for traveling-wave tubes [J]. AEU-INTERNATIONAL JOURNAL OF ELECTRONICS AND COMMUNICATIONS, 2016, 70(10): 1412-6.
[23] CHANG Z W, SHU G X, TIAN Y Y, et al. A Broadband Extended Interaction Klystron Based on Multimode Operation [J]. IEEE TRANSACTIONS ON ELECTRON DEVICES, 2022, 69(2): 802-7.
[24] CHANG Z W, SHU G X, TIAN Y Y, et al. A Multimode Extended Interaction Oscillator With Broad Continuous Electric Tuning Range [J]. IEEE TRANSACTIONS ON ELECTRON DEVICES, 2022, 69(7): 3947-52.
[25] SHI N J, ZHANG C Q, WANG S M, et al. A Novel Scheme for Gain and Power Enhancement of THz TWTs by Extended Interaction Cavities [J]. IEEE TRANSACTIONS ON ELECTRON DEVICES, 2020, 67(2): 667-72.
[26] GILMOUR A S. Klystrons, Traveling Wave Tubes, Magnetrons, Cross-Field Amplifiers, and Gyrotrons [C]. 2011.
[27] KOWALCZYK R, ZUBYK A, MEADOWS C, et al. A 100 Watt W-Band MPM TWT [C]. 2013 IEEE 14TH INTERNATIONAL VACUUM ELECTRONICS CONFERENCE (IVEC). 2013.
[28] ZHANG X Q, FENG J J, CAI J, et al. Design and Experimental Study of 250-W W-band Pulsed TWT With 8-GHz Bandwidth [J]. IEEE TRANSACTIONS ON ELECTRON DEVICES, 2017, 64(12): 5151-6.
[29] XU C, MENG L, PAOLONI C, et al. A 0.35-THz Extended Interaction Oscillator Based on Overmoded and Bi-Periodic Structure [J]. IEEE TRANSACTIONS ON ELECTRON DEVICES, 2021, 68(11): 5814-9.
[30] CST: Darmstadt, Germany, 2020.
[31] QU Z W, ZHANG Z Q, GUO N N, et al. Demonstration of a G-Band High-Power Extended Interaction Klystron [J]. IEEE ELECTRON DEVICE LETTERS, 2023, 44(10): 1736-9.
[32] PETER R, FISCHERAUER G. Measurement of Axially Inhomogeneous Permittivity Distributions in Resonant Microwave Cavities [J]. IEEE TRANSACTIONS ON MICROWAVE THEORY AND TECHNIQUES, 2019, 67(6): 2433-42.
[33] MORAWSKI T. Application of the Perturbation Method in Some Microwave Measurements [J]. IEEE Transactions on Instrumentation and Measurement, 1970, vol. 19, no. 4, pp. 373-376, Nov 1970.
[34] CORBELLINI S, GAVIOSO R M. A Low-Cost Instrument for the Accurate Measurement of Resonances in Microwave Cavities [J]. IEEE TRANSACTIONS ON INSTRUMENTATION AND MEASUREMENT, 2013, 62(5): 1259-66.
[35] SYDORUK V A, FIORANI F, JAHNKE S, et al. Design and Characterization of Microwave Cavity Resonators for Noninvasive Monitoring of Plant Water Distribution [J]. IEEE TRANSACTIONS ON MICROWAVE THEORY AND TECHNIQUES, 2016, 64(9): 2894-904.
[36] CONNOLLY D J. Determination of the Interaction Impedance of Coupled Cavity Slow Wave Structures [J]. IEEE Transactions on Electron Devices. 1976.
[37] XU C, MENG L, YIN Y, et al. Demonstration of the Electronic Cutoff Field in Millimeter-Wave Extended Interaction Oscillators [J]. IEEE TRANSACTIONS ON ELECTRON DEVICES, 2021, 68(5): 2473-9.